Designing covalent organic frameworks with Co-O$_4$ atomic sites for efficient CO$_2$ photoreduction

Qian Zhang [1,4], Shuaiqi Gao [1,4], Yingying Guo[1], Huiyong Wang [1] ✉, Jishi Wei [2], Xiaofang Su [1], Hucheng Zhang [1], Zhimin Liu [3] ✉ & Jianji Wang [1] ✉

Cobalt coordinated covalent organic frameworks have attracted increasing interest in the field of CO$_2$ photoreduction to CO, owing to their high electron affinity and predesigned structures. However, achieving high conversion efficiency is challenging since most Co related coordination environments facilitate fast recombination of photogenerated electron-hole pairs. Here, we design two kinds of Co-COF catalysts with oxygen coordinated Co atoms and find that after tuning of coordination environment, the reported Co framework catalyst with Co-O$_4$ sites exhibits a high CO production rate of 18000 μmol g^{-1} h^{-1} with selectivity as high as 95.7% under visible light irradiation. From in/ex-situ spectral characterizations and theoretical calculations, it is revealed that the predesigned Co-O$_4$ sites significantly facilitate the carrier migration in framework matrixes and inhibit the recombination of photogenerated electron-hole pairs in the photocatalytic process. This work opens a way for the design of high-performance catalysts for CO$_2$ photoreduction.

Over the past half century, the atmospheric concentration of CO$_2$ has increased steadily because of the excessive consumption of fossil fuels and the continuous discharge of CO$_2$, causing disastrous environmental problems, such as global warming and ecological deterioration[1,2]. As a result, CO$_2$ neutralization technologies are urgently required to alleviate the pressures of both the existing high atmospheric CO$_2$ level and the continuous increment in CO$_2$ emissions[3,4]. A photocatalytic CO$_2$ reduction reaction (CO$_2$RR) has been considered an environmentally friendly solution for these problems, as light is clean, noninvasive, and remote-controllable. To date, the most used photocatalysts for the CO$_2$RR are metal oxides[5,6], sulfides[7], polyoxometalates (POMs)[8], metal-organic frameworks (MOFs)[9], and conjugated microporous polymers[10]. Despite the promise of these photocatalysts, the production and selectivity of reaction products are quite low due to three essential limitations—poor light absorption efficiency, fast recombination of photogenerated electron-hole pairs, and less efficacious active sites— which often result in undesired side reactions[11]. Therefore, seeking more efficient photocatalysts is of great significance to overcome these obstacles.

Covalent organic framework (COF) is a class of organic polymers linked by reversible covalent bonds. COFs have highly periodic and modular crystalline structures, defining their programmable characteristics[12]. Recently, these porous frameworks have emerged as potential candidates for photocatalytic CO$_2$RR to CO due to their large surface areas, astonishing π-conjugated skeletons, high chemical and thermal stabilities, tuneable pore sizes, and functionalities[13–15]. To enhance the photocatalytic activity of the parent COF, several strategies have been developed in recent years. Among these

[1]Key Laboratory of Green Chemical Media and Reactions (Ministry of Education), Collaborative Innovation Centre of Henan Province for Green Manufacturing of Fine Chemicals, School of Chemistry and Chemical Engineering, Henan Normal University, Xinxiang, Henan 453007, P. R. China. [2]Department of Electrical and Computer Engineering, National University of Singapore, Singapore 117583, Singapore. [3]Beijing National Laboratory for Molecular Sciences, Key Laboratory of Colloid, Interface and Thermodynamics, CAS Research/Education Centre for Excellence in Molecular Sciences, Institute of Chemistry, Chinese Academy of Sciences, Beijing 100190, P. R. China. [4]These authors contributed equally: Qian Zhang, Shuaiqi Gao. ✉e-mail: hywang@htu.edu.cn; liuzm@iccas.ac.cn; jwang@htu.edu.cn

strategies, incorporating metal sites into the host frameworks of COF is a feasible and compelling method for improving the photocatalytic activity since it increases the number of active sites, facilitates electron transfer into the COF, and enhances the separation efficiency of photogenerated electron-hole pairs[15]. Nevertheless, when considering the chemical microenvironments integrated with metal and local binding modes[16], different metal coordination sites, such as metal-N_4[17], metal-N_3O[18], metal-N_2O_2[10], and metal-N_4O[19], often exhibit distinct performance characteristics for photocatalytic CO_2RR. Unfortunately, the related structure-activity relationship is not clear, which results in a large deviation in the design of high-efficiency CO_2 photoreduction catalysts. Therefore, the most significant consideration is to establish guidelines for a clear functional description of the metal-coordination centers, which is the core thought for understanding how to design a metal-COF catalyst with high efficiency[17]. In addition, the optimal coordination environments of metal centers in the COF matrixes are essential factors for catalyst design, as they determine the activities of metal sites[20].

To this end, a programmable design approach, as a strategy for dividing complex systems into more manageable modules[21], is usually used in the programmable chemical synthesis of reticular materials and offers a good opportunity to regulate the chemical microenvironments of metal-COF composites with specific purposes and rationalities[12,22]. Guided by this approach, metal-COF composites with modular structures are regarded as good platforms for CO_2 photochemical conversion, which involves various rigid secondary units, such as organic functional groups and metal sites[12,23,24]. By means of the programmable approach, these basic structural modules may be selected and optimized to modulate the microenvironments for the catalysis[25]. However, using the programmable approach to design desired coordination modes in well-defined COF remains unexplored.

In this work, we design two types of cobalt Schiff base COF composites for the photocatalytic CO_2RR to CO, in which cobalt is anchored by coordinated oxygen atoms. Benefiting from the controllable functional groups in the precursor modules and the strong coordination of cobalt (II)[26], the cobalt-COF (Co-COF) was spontaneously formed according to the predesigned position of the -OH group in aldehyde modules by a programmable approach to provide precise coordination microenvironments. Through various spectral characterizations and theoretical calculations, a distinct Co-O_4 coordination mode is identified. The corresponding Co-COF composite exhibits a remarkably high CO production rate of 18000 $\mu mol\ g^{-1}\ h^{-1}$ and an excellent CO selectivity of 95.7%. The CO production rate is higher than and the selectivity is comparable to the current record reported for metal-COF photocatalysts[15,27,28]. Mechanistic investigations indicate that the supereminent photocatalytic performance of Co-COF with Co-O_4 sites

is mainly attributed to the strong separation ability of photoinduced electrons and holes although the contributions of high CO_2 adsorption capacity and low charge-transfer resistance are also important.

Results

Construction and analysis of microenvironments

Here, 2,4,6-tris(4-aminophenyl)−1,3,5-triazine (TAPT) was used as a fixed module, and different aldehyde molecules were selected to serve as modules for building different porous frameworks containing isolated Co sites (Co-X-COF, where X represents aldehyde modules used to synthesize different COF matrixes, such as 2,3-dihydroxybenzene-1,4-dicarboxaldehyde (2,3-DHTA) and 2,4,6-trihydroxybenzene-1,3,5-tricarbaldehyde (TP)). Specifically, 2,3-DHTA was employed to form Co-O_4 sites, while TP was applied to generate Co-O_3N sites for comparative studies on different chemical environments. The structures of the parent COF and corresponding Co-COF are shown in Fig. 1 and Supplementary Fig. 1. For comparison, related characterizations for X-COF samples without Co sites were performed.

Fourier transform infrared (FTIR) spectroscopy was employed to study the structural features of different frameworks. By using Co-2,3-DHTA-COF and its precursor modules as an example, the C = N stretching vibration peak was observed at 1623 cm^{-1}, which refers to the formation of an imine bond between the 2,3-DHTA and TAPT modules, and accompanied by the vanishing of the amino band in the TAPT module (at approximately 3460, 3303, and 3209 cm^{-1}) and the disappearance of the carbonyl band in the 2,3-DHTA module (at 1654 cm^{-1})[13,29] (Fig. 2a and Supplementary Fig. 2a). This result indicated the successful construction of the 2,3-DHTA-COF matrix. After incorporating Co (II) into the COF matrix, the peak of C-O at 1291 cm^{-1}, which was attributed to the stretching vibration of the phenoxy group in 2,3-DHTA modules[30], was blueshifted to 1298 cm^{-1}. At the same time, the new peaks at 1459 and 1347 cm^{-1} appeared for C-O-Co[31,32] (Fig. 2a), providing direct evidence for the Co coordination environment. Likewise, the FTIR spectra of Co-TP-COF exhibited a similar trend in the change in the C-O vibration peak (Supplementary Fig. 2b). Solid-state ultraviolet-visible (UV-vis) diffuse reflection spectra showed that the absorption edges of Co-COF exhibited apparent redshifts relative to those of the parent COF matrixes (Supplementary Fig. 3), which was in line with the FTIR results and supported the formation of Co coordination centers.

The powder X-ray diffraction (PXRD) patterns of 2,3-DHTA-COF and Co-2,3-DHTA-COF are shown in Fig. 2b. A sharp diffraction peak at 2.89° appeared with three broad peaks at 4.85°, 5.72°, and 7.61°, corresponding to the (100), (110), (200) and (210) planes of 2,3-DHTA-COF[29], respectively, which was in good agreement with the PXRD simulation result (Fig. 2b). However, no diffraction peaks of cobalt

2,3-DHTA-COF   **Co-2,3-DHTA-COF**

2,3-DHTA
&
TAPT
Precursors

Step 1 Solvothermal Reactions   Step 2 Adding **Co(NO₃)₂** in H_2O/C_2H_5OH
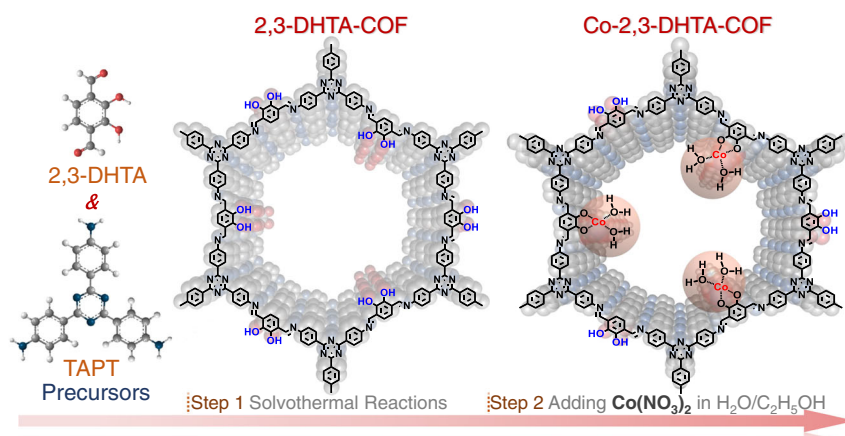
Fig. 1 | Schematic illustration of the synthesis of 2,3-DHTA-COF and Co-2,3-DHTA-COF as typical examples. In this study, TAPT works as the fixed module and 2,3-DHTA serves as the test module.
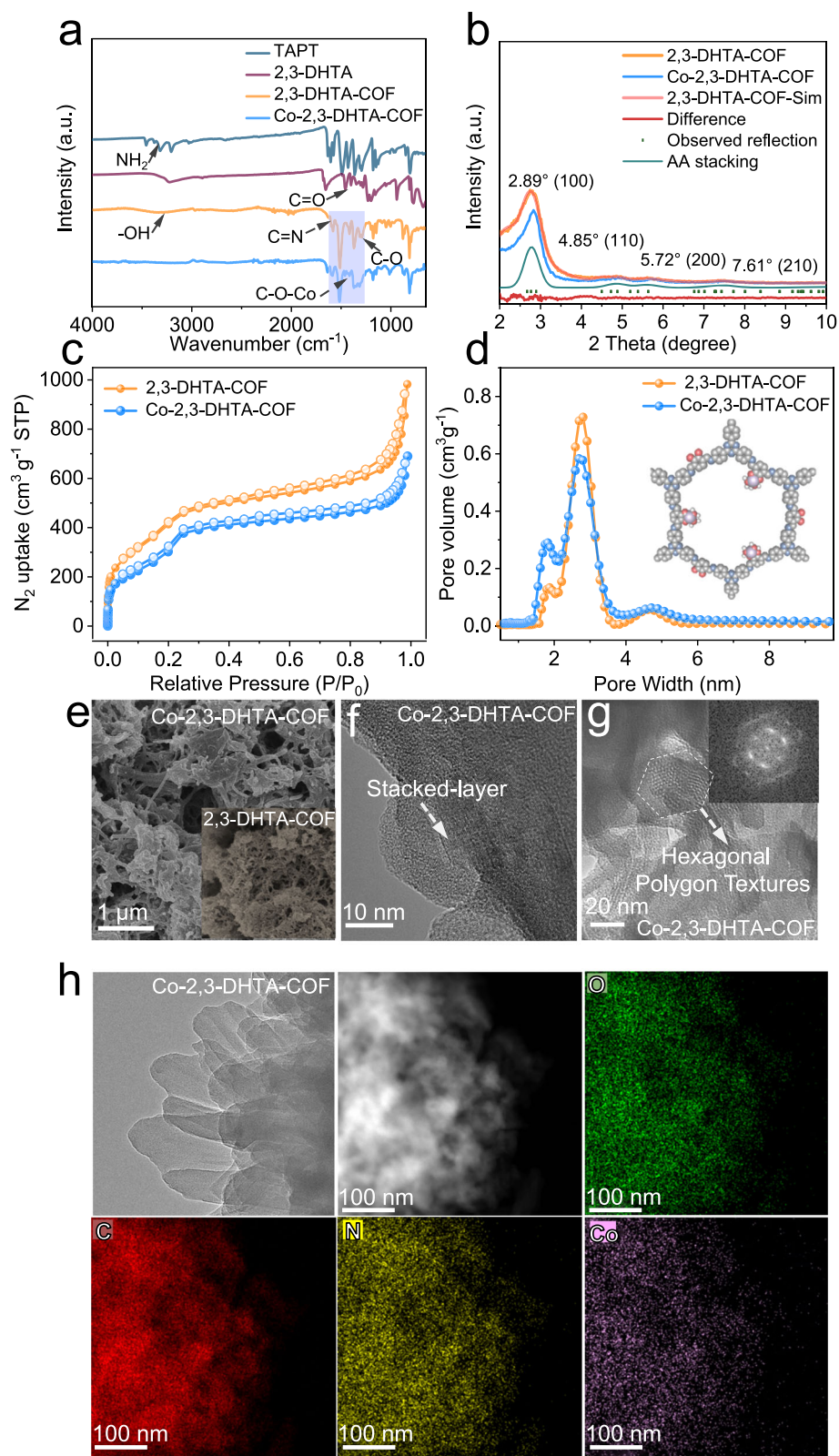
Fig. 2 | Spectral and structural comparison of 2,3-DHTA-COF and Co-2,3-DHTA-COF. a FTIR spectra. **b** Experimental and simulated X-ray diffraction (XRD) patterns. **c** N_2 adsorption-desorption isotherms. **d** Pore size distribution calculated by the non-local density functional theory (NLDFT) model. **e** SEM images. **f**–**g** High-resolution TEM images. **h** Energy dispersive X-ray (EDX) maps of Co-2,3-DHTA-COF, with oxygen mapped in green, carbon mapped in red, nitrogen mapped in yellow, and cobalt mapped in purple. Scale bar: 100 nm.

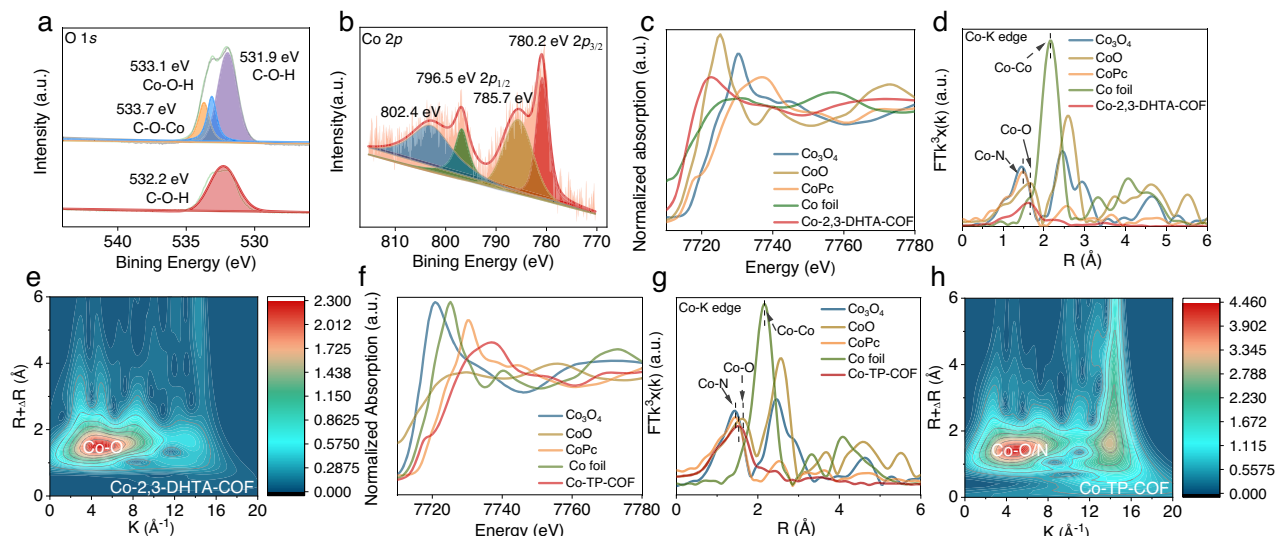**Fig. 3 | Coordination environment analysis. a** High-resolution XPS spectra of O 1s in Co-2,3-DHTA-COF and 2,3-DHTA-COF. **b** High-resolution XPS spectra of Co 2p in Co-2,3-DHTA-COF. **c**, **d** Normalized XANES spectra and FT-EXAFS spectra at the Co k-edge of Co-2,3-DHTA-COF, Co_3O_4, CoO, CoPc and Co foil samples. **e** WT-EXAFS spectrum of discriminating radial distance and k-space resolution of Co-2,3-DHTA-COF. **f** Normalized XANES spectra. **g** FT-EXAFS spectra. **h** WT-EXAFS spectrum for discriminating the radial distance and k-space resolution of Co-TP-COF.

nanoparticles or cobalt salt were observed, suggesting that cobalt existed in the form of a coordination structure rather than in the form of cobalt salt or metallic cobalt nanoparticles in the COF matrix[10]. The same conclusion applied to Co-TP-COF (Supplementary Fig. 4). In addition, the PXRD simulation results indicated that the crystal structure was in AA stacking[29,33]. From the N_2 adsorption isotherms (Fig. 2c, d), the incorporation of Co (II) into the parent COF decreased the surface area, but the pore size remained unchanged in the Co-COF. For example, the specific surface area was 1050 $m^2\,g^{-1}$ for 2,3-DHTA-COF and 769 $m^2\,g^{-1}$ for Co-2,3-DHTA-COF, while the pore size was 2.70 nm for both the COF and the Co-COF. A similar trend was observed for TP-COF and Co-TP-COF (Supplementary Fig. 5).

From the scanning electron microscopy (SEM) images (Fig. 2e and Supplementary Fig. 6), the COF and Co-COF showed predominantly ribbon-like morphologies[34]. In addition, the transmission electron microscopy (TEM) and high-resolution TEM images of Co-2,3-DHTA-COF (Fig. 2f, g and Supplementary Fig. 7) exhibited a stacked-layer structure with an interlayer spacing of 0.3 nm and hexagonal polygon pores with pore sizes of 2.6 nm. As the energy dispersive X-ray (EDS) maps suggested, cobalt (II) was homogeneously distributed throughout the COF matrix without any precipitation on the surface (Fig. 2h).

The coordination environment of cobalt (II) in the 2,3-DHTA-COF matrix was investigated by X-ray photoelectron spectroscopy (XPS) (Supplementary Fig. 8). In detail, the O 1s peak of Co-2,3-DHTA-COF was deconvoluted into three peaks (Fig. 3a): one at 531.9 eV for C-O-H[35], one at 533.1 eV for Co-O-H and one at 533.7 eV for C-O-Co[10]. 2,3-DHTA-COF would exhibit a typical C-O-H peak at 532.2 eV[36]. Thus, the C-O-H peak shift (from 532.2 to 531.9 eV) and the new C-O-Co peak appearance (at 533.7 eV) suggested that the oxygen atom in Co-2,3-DHTA-COF was bonded with cobalt (II)[10]. A similar result was found for Co-TP-COF (Supplementary Fig. 9). In addition, no peak was observed for $[NO_3]^-$ in $Co(NO_3)_2\cdot6H_2O$ at 407.0 eV[37,38]. Nevertheless, the N 1s peak of Co-2,3-DHTA-COF was deconvoluted into two peaks (Supplementary Fig. 8e), one at 399.1 eV for C-N and the other at 401.1 eV for C=N[30], and no N-O peak was found. These results indicated that nitrate was not present in the Co-COF. Therefore, the oxygen of $[NO_3]^-$ did not participate in the $Co-O_4$ coordination. In addition, the Co $2p_{3/2}$ and Co $2p_{1/2}$ binding energies at 780.2 and 796.5 eV (Fig. 3b) illustrated the +2 oxidation state of Co in Co-2,3-DHTA-COF[39], and the same conclusion was drawn from the XPS spectrum of Co-TP-COF

(Supplementary Fig. 9). Inductively coupled plasma–mass spectrometry (ICP–MS) showed that the cobalt contents in Co-2,3-DHTA-COF and Co-TP-COF were approximately 2.14 and 1.05 wt.%, respectively, which was the maximum cobalt loading in the COF matrix. This high Co loading of Co-2,3-DHTA-COF indicated that the 2,3-DHTA module provided a more favorable coordination microenvironment for cobalt (II), which was consistent with the XPS analysis data (Supplementary Table 1). However, the cobalt contents in these two Co-COFs were much lower than the theoretical values (10.8 wt.% for Co-2,3-DHTA-COF and 9.4 wt.% for Co-TP-COF), suggesting that only a fraction of oxygen atoms in the Co-COF were bonded with cobalt (II)[10,30].

A more accurate coordination environment of the cobalt species was disclosed by synchrotron-radiation-based X-ray absorption spectroscopy (XAS) analysis. X-ray absorption near-edge structure (XANES) spectra acquired for Co-2,3-DHTA-COF, Co-TP-COF, and the standard references (cobalt foil, CoO, CoPc (cobalt phthalocyanine), and Co_3O_4) are presented in Fig. 3c–e and Supplementary Figs. 10 and 11. For Co-2,3-DHTA-COF, the near-edge shoulder was at the same position as that for CoO, implying that the Co species were divalent in Co-2,3-DHTA-COF, which was in agreement with the result from XPS analysis. Moreover, the Fourier transformed extended X-ray absorption fine structure (FT-EXAFS) spectrum of Co-2,3-DHTA-COF in R space exhibited a dominant Co-O peak at 1.61 Å (Fig. 3d). This result was similar to the Co-O bond of the standard CoO in the range of 1.6−1.7 Å but different from the characteristic peak of the Co-Co bond (cobalt foil) at 2.16 Å or the Co-N bond (CoPc) at 1.45 Å. Accordingly, this result showed that the cobalt centers in the Co-2,3-DHTA-COF were surrounded by the oxygen atoms of the 2,3-DHTA aldehyde modules. More importantly, there were no other peaks of Co-2,3-DHTA-COF that were observed in the range of 2.3-3.0 Å, such as those of Co-O and Co-Co in the standard cobalt foil, CoO, and Co_3O_4 samples. Therefore, the above results corroborated that the cobalt-oxygen coordination structure was the only existing form of cobalt in Co-2,3-DHTA-COF.

The specific coordination number and hyperfine structure around the cobalt centers were investigated by fitting the EXAFS data for the first coordination shell of Co-2,3-DHTA-COF (Supplementary Fig. 10). Each cobalt atom was coordinated by four O atoms ($Co-O_4$), and the average bond length of Co-O was 2.09 Å in the first shell (Supplementary Table 2). As shown in the wavelet transform (WT) contour plots of Co-2,3-DHTA-COF (Fig. 3e), the contour maximum was

detected at 5 Å^{-1} (abscissa), and the main peak was at approximately 1.5 Å (ordinate), which corresponded to the Co-O coordination in the first shell. In addition, no maximum intensity of the Co-Co contribution was observed in the second shell at approximately 2.9 Å, providing additional evidence for the absence of the Co-Co bond in Co-2,3-DHTA-COF[26,40]. Relative to the coordination mode of Co (II) in Co-2,3-DHTA-COF, the peak position and intensity of Co-TP-COF in R space changed simultaneously, and the strong peak (1.53 Å) between the Co-N (1.45 Å) and Co-O (1.65 Å) peaks was confirmed to be Co-O$_3$N. This difference in the cobalt (II) coordination mode between Co-2,3-DHTA-COF and Co-TP-COF fit well with the logic for microenvironment design via the regulation of the precursor aldehyde modules (Fig. 3f–h, Supplementary Fig. 10 and Table 2).

In order to determine whether the water molecules in Co(NO$_3$)$_2$·6H$_2$O participated in Co-O coordination, thermogravimetric analysis (TGA) of the two Co-COFs was conducted. Interestingly, thermal peaks of crystalline water[41–43] were observed at 217 and 249 °C from the first derivative of the TGA curves for Co-2,3-DHTA-COF and Co-TP-COF, respectively (Supplementary Fig. 12), suggesting that water molecules in Co(NO$_3$)$_2$·6H$_2$O existed in the Co-COFs. Combined with the above results, the oxygen atoms of Co-O$_4$ in Co-2,3-DHTA-COF clearly came from water molecules and the framework of 2,3-DHTA-COF because the coordination of [NO$_3$]$^-$ towards Co (II) was ruled out. To examine oxygen species from the framework in Co-O$_4$, we conducted infrared and solid hydrogen−1 nuclear magnetic resonance (^{1}H NMR) studies on Co-2,3-DHTA-COF and 2,3-DHTA-COF. Unfortunately, we failed to obtain any useful information due to the low content of Co (II) in Co-2,3-DHTA-COF and the low sensitivity of solid ^{1}H NMR and infrared spectroscopy.

By considering the structural similarity of phenolic hydroxyl groups in 2,3-dihydroxybenzene−1,4-dicarboxaldehyde (one of the building blocks for the preparation of the Co-COF) to that in 2,3-DHTA-COF and the high sensitivity of liquid ^{1}H NMR technology, we determined the ^{1}H NMR spectra of 2,3-dihydroxybenzene-1,4-dicarboxaldehyde and Co-2,3-dihydroxybenzene-1,4-dicarboxaldehyde complex in d^6-dimethyl sulfoxide (DMSO), where Co-2,3-dihydroxybenzene-1,4-dicarboxaldehyde complex was prepared under the same conditions as Co-2,3-DHTA-COF. Supplementary Fig. 13 showed that the peak at 10.72 ppm was ascribed to the phenolic hydroxyl protons of 2,3-dihydroxybenzene-1,4-dicarboxaldehyde, and the number of hydrogen atoms obtained by the area integral was 2. However, this peak weakened, and the number of hydrogen atoms was 1.6 in the Co-2,3-dihydroxybenzene−1,4-dicarboxaldehyde complex. This result indicated that a fraction of hydrogen in the phenolic hydroxyl groups of the Co-2,3-dihydroxybenzene−1,4-dicarboxaldehyde complex was lost to provide oxygen anions (deprotonated phenolic hydroxyl groups) in the presence of Co (II). Similar metal complexes in DMSO were also reported in the literature[42].

From the above analyzes, the two adjacent oxygen anions in the COF frameworks were coordinated with Co (II). In this case, it was not possible for [NO$_3$]$^-$ to coordinate Co (II) in the Co-COF because of the requirement of electroneutrality. Again, this result showed that [NO$_3$]$^-$ was not involved in the Co-O$_4$ coordination. Then, oxygen atoms from two H$_2$O molecules were coordinated towards Co (II), which was supported by the thermal peaks of crystalline water observed for Co-2,3-DHTA-COF. Therefore, it was appropriate to state that the Co-O$_4$ coordination mode was formed by two adjacent oxygen anions from Co-COF and two oxygen atoms from two H$_2$O molecules, as shown in Fig. 1.

Photocatalytic performance of CO$_2$ to CO

In principle, when the bandgap of the COF was lower than the redox potential of the CO$_2$RR, the COF can be used as the catalyst for the CO$_2$RR. From the UV–vis diffuse reflectance spectra of the Co-COF catalysts (Supplementary Fig. 3), the optical bandgaps of Co-2,3-DHTA-COF and Co-TP-COF were 1.60 and 2.17 eV, respectively (Supplementary Fig. 14). Mott-Schottky plots showed that these two Co-COFs were n-type semiconductors with typical positive slopes (Supplementary Fig. 15), and the conduction band minimum (CBM) edges of Co-2,3-DHTA-COF and Co-TP-COF at pH = 7 were calculated to be −0.67 and −0.84 V (vs. normal hydrogen electrode (NHE)), respectively (Supplementary Fig. 16a). Therefore, the CBM potentials (−0.67 and −0.84 V) of these two Co-COFs were lower than the redox potential of CO$_2$ to CO (−0.53 V) but much higher than the lowest unoccupied molecular orbital energy level (−1.31 V vs. NHE) of the photosensitizer [Ru(bpy)$_3$]Cl$_2$. Thus, the photoinduced electrons transferred from the photosensitizer [Ru(bpy)$_3$]Cl$_2$ to Co-COF, and the CO$_2$RR was thermodynamically feasible (Supplementary Fig. 16b).

Based on the above results, we performed photocatalytic CO$_2$RR experiments in acetonitrile (MeCN)/water mixed solution under simulated visible light irradiation (λ ≥ 420 nm), with [Ru(bpy)$_3$]Cl$_2$ and triethanolamine (TEOA) as the potential photosensitizer and electron donor, respectively. Before estimating the CO$_2$ photocatalytic performance of the Co-COF, a series of control experiments were performed to optimize the photocatalytic reaction conditions. The results are given in Fig. 4a–c. It was found from Fig. 4a and Supplementary Fig 17 that no CO was produced without visible light, TEOA or Co-2,3-DHTA-COF, and H$_2$ was detected in the presence of TEOA and [Ru(bpy)$_3$]Cl$_2$ but no Co-2,3-DHTA-COF. Only in the presence of Co-2,3-DHTA-COF and TEOA, a small amount of CO and H$_2$ were observed. However, when [Ru(bpy)$_3$]Cl$_2$ and Co-2,3-DHTA-COF simultaneously existed in the system, the CO production was greatly improved. These results indicated that [Ru(bpy)$_3$]Cl$_2$, Co-2,3-DHTA-COF, and TEOA worked as photosensitizers, photocatalysts and electron donors, respectively. Moreover, the effects of other factors, such as the ratio of acetonitrile/water and the photocatalyst amount, on photocatalytic activity and CO selectivity were explored to provide the best photocatalytic conditions. The optimized volume ratio of acetonitrile/water was clearly 4:1 (Fig. 4b), and 1.00 mg of catalyst loading was adopted to improve CO selectivity although the best production rate was observed at a dose of 0.50 mg (Fig. 4c and Supplementary Fig. 18). A similar catalyst dosage was often used in previous photocatalytic studies[10,13,40,44]. Under the optimized conditions, CO$_2$RR to CO was performed, and the gaseous and liquid products in the photocatalytic reduction system were detected by gas chromatography and ^{1}H NMR spectroscopy, respectively. H$_2$ and CO were detected in the gaseous products, but no liquid product was detectable (Supplementary Figs. 19 and 20).

Figure 4d displays the variation in CO and H$_2$ production with reaction time using the Co-2,3-DHTA-COF catalyst. The CO production was continuously produced in the initial 4 h, but the production rate significantly decreased after 1 h upon light illumination. This retardation effect was attributed to the degradation of the photosensitizer [Ru(bpy)$_3$]Cl$_2$, as evaluated from the obvious decrease in its light absorption intensity (Supplementary Fig. 21). A similar phenomenon was reported in previous photocatalysis investigations[45–47]. Supplementary Fig. 22 displays the CO and H$_2$ production from the CO$_2$RR catalyzed by the Co-COF and the parent COF for 4 h under the same conditions. Notably, the optimal Co-2,3-DHTA-COF showed a very high CO production rate of 18,000 μmol g^{-1} h^{-1} with a H$_2$ production rate of 800 μmol g^{-1} h^{-1} (Supplementary Tables 3 and 4). Thus, the selectivity towards the CO product was 95.7%, and the relevant turnover frequency (TOF) reached 111.8 h^{-1}. The CO production rate of Co-2,3-DHTA-COF was 23.6 times that of 2,3-DHTA-COF. Compared with the COF-based catalysts reported in the literatures, the optimal Co-2,3-DHTA-COF offered a higher CO production rate than the current record reported in the photocatalytic CO$_2$RR-to-CO as well as comparable CO selectivity (Supplementary Table 5). However, Co-TP-COF exhibited a lower production rate (11,600 μmol g^{-1} h^{-1}) and selectivity (76.6%) for CO. To exclude the effects of the cobalt contents of the two Co-COFs on their catalytic performance levels, the Co-2,3-DHTA-COF
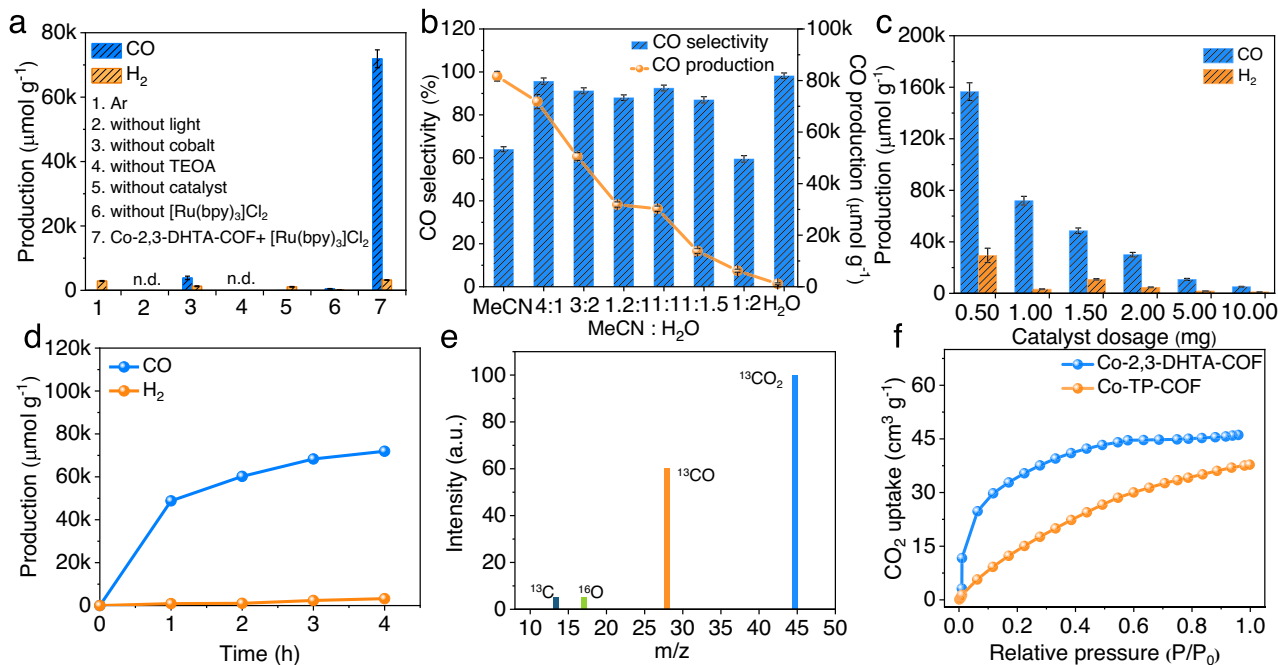
Fig. 4 | Optimization of the catalytic conditions using Co-2,3-DHTA-COF as the catalyst. a Control experiments of catalytic conditions. **b** Effect of the acetonitrile/H_2O volume ratio on the photocatalytic CO_2RR. **c** Dependence of catalyst mass loading on CO and H_2 production within 4 h. **d** CO and H_2 evolution with irradiation time for the CO_2RR catalyzed by Co-2,3-DHTA-COF under visible light irradiation. **e** Gas chromatography–mass spectrometry for ^{13}C isotope tracer tests. **f** CO_2 adsorption isotherms of the two Co-COFs at 25 °C. The error bars for the production and selectivity uncertainty of CO and H_2 represent one standard deviation based on three independent samples.

sample with a cobalt content of 1.12 wt.%, which was similar to that in Co-TP-COF (1.05 wt.%), was prepared and applied for the photocatalytic CO_2RR to CO. A CO production rate of 13,900 μmol g^{-1} h^{-1} and a selectivity of 90.4% were achieved, indicating that the different catalytic performance levels of Co-2,3-DHTA-COF and Co-TP-COF were mainly caused by the difference in Co coordination modes. Obviously, the Co-O$_4$ site significantly improved the catalytic performance of Co-COF for the CO_2RR to CO, which was in good agreement with our design goals.

The apparent quantum efficiency (AQE) of the CO_2 photocatalytic process over Co-2,3-DHTA-COF was then studied at various wavelengths, and the variety of AQE values with wavelengths followed the characteristic absorption spectrum of [Ru(bpy)$_3$]Cl$_2$ (Supplementary Fig. 23). The highest AQE value was 0.47% at 450 nm (Supplementary Table 6). These results confirmed that [Ru(bpy)$_3$]Cl$_2$ functioned as the photosensitizer in this work. In addition, the produced ^{13}CO (m/z = 29) detected by gas chromatography–mass spectrometry (Fig. 4e) verified that the generated CO came from CO_2 rather than the other organic molecules, such as the photosensitizer [Ru(bpy)$_3$]Cl$_2$, electron donor triethanolamine and COF matrix.

Encouraged by the above results, we evaluated the photocatalytic reduction performance of Co-2,3-DHTA-COF for low-concentration CO_2. To this end, 10 vol.% CO_2 (a typical CO_2 concentration in the exhaust gas of coal-fired power plants) in N_2 was taken for a 4 h conversion. The optimal Co-COF still exhibited an excellent CO production rate of 9600 μmol g^{-1} h^{-1} (Supplementary Fig. 24a), which even exceeded the values of many other metal-COF catalysts in a pure CO_2 atmosphere (Supplementary Table 5). Although the selectivity of CO decreased and the production rate of H_2 was more than twice that of CO, this H_2-CO mixed gas was the so-called syngas that was an important raw material for the industrial synthesis of high value-added chemicals.

Moreover, natural sunlight irradiation was used for the photocatalytic CO_2RR to CO under reaction conditions similar to those mentioned above. For this purpose, a 4-h photocatalytic reaction (from 10:0 am to 14:0 pm) per day was conducted for 3 consecutive days in December on outdoors of the campus at the location of east longitude 113°54'46" and north longitude 35°19'46". Remarkably, on sunny days in winter, the average production rate of the photocatalytic CO_2RR to CO catalyzed by Co-2,3-DHTA-COF reached 11000 ± 20 μmol g^{-1} h^{-1}, and the selectivity towards CO reached 89% (Supplementary Fig. 24b). Considering the low temperature (approximately 19 °C) and weak light intensity (less than 50 mW cm^{-2}) during testing (Supplementary Fig. 24c, d and Table 7), such a high CO production rate and selectivity indicated that with the advantages in the microenvironment of Co-2,3-DHTA-COF, natural sunlight was utilized for photocatalytic CO_2RR to CO with effect, highlighting the high potential of the programmable approach in the design of specific microenvironments for practical applications.

In addition, to examine the stability of Co-2,3-DHTA-COF in CO_2 photocatalytic reduction to CO, fresh [Ru(bpy)$_3$]Cl$_2$ was added to the system after each cycle to maintain a continuous process for the catalytic reaction. The good photocatalytic stability of Co-2,3-DHTA-COF was verified in three CO_2 reduction cycle tests with a slight deterioration (Supplementary Fig. 25). Furthermore, the good chemical stability of Co-2,3-DHTA-COF was confirmed by comparing its TEM images, FTIR spectra, PXRD patterns, and XPS spectra before and after the catalytic process (Supplementary Figs. 26 and 27).

Reaction mechanism

The high photocatalytic CO_2 reduction performance of Co-2,3-DHTA-COF inspired us to investigate the CO_2 photoreduction mechanism by isothermal CO_2 adsorption, various ex/in situ spectral measurements, and density functional theory (DFT) calculations. Since CO_2 adsorption was the first action before the catalytic steps, we first studied the adsorption isotherm of CO_2 on the parent COF and Co-COF. The CO_2 adsorption capacities of Co-2,3-DHTA-COF and Co-TP-COF were 46.1 and 37.8 cm^3 g^{-1} (Fig. 4f and Supplementary Fig. 28), which were

3.8 times that of 2,3-DHTA-COF and 1.2 times that of TP-COF, respectively. The higher CO_2 adsorption capacity of Co-2,3-DHTA-COF was attributed to its chemisorption for CO_2 through the stronger coordination interaction of CO_2 with Co (II) where the CO_2 desorption peak was observed at -212 °C, while the CO_2 adsorption of 2,3-DHTA-COF was physical in nature[48,49] since its CO_2 desorption peak was observed at approximately 80 °C, as determined by a temperature-programmed CO_2 desorption experiment (Supplementary Fig. 29). In addition, although the CO_2 adsorption capacity of TP-COF ($33.5\ cm^3\ g^{-1}$) was significantly higher than that of 2,3-DHTA-COF ($12.8\ cm^3\ g^{-1}$), the CO_2 adsorption capacity of Co-TP-COF was less than that of Co-2,3-DHTA-COF. Given that 2,3-DHTA-COF and TP-COF had the same topological structure, this result suggested that $Co\text{-}O_4$ coordination in 2,3-DHTA-COF, rather than the topological structure, played a crucial role in the enhancement of CO_2 adsorption capacity. Benefiting from the microenvironment constructed by the 2,3-DHTA modules, the optimal Co-2,3-DHTA-COF exhibited a high capacity CO_2 adsorption, which was favorable for the CO_2RR to CO.

It is known that upon illumination with visible light, the electrons in semiconducting materials could move to the conduction band to create holes in the valence band. The electron-hole separation efficacy was one of the most important factors for CO_2 reduction. Thus, the photogenerated electron-hole separation efficiency was determined by photoluminescence (PL) spectroscopy. The steady-state PL spectra (Supplementary Fig. 30a) indicated that the strong emission of the photosensitizer $[Ru(bpy)_3]Cl_2$ was effectively quenched in the presence of Co-COF/COF, while the PL spectrum of $[Ru(bpy)_3]Cl_2$ was not quenched with various amounts of the sacrificial agent TEOA (Supplementary Fig. 31a), as reported previously[50]. However, with the addition of Co-2,3-DHTA-COF, the PL spectrum of the excited $[Ru(bpy)_3]Cl_2$ was gradually quenched, but there was almost no influence on the visible absorption spectrum of $[Ru(bpy)_3]Cl_2$ (Supplementary Fig. 31b, c). This result suggested that the PL spectrum directly quenched by Co-2,3-DHTA-COF in the photocatalytic system was not static quenching because static quenching, along with the formation of complexes between the luminophore and quencher, usually resulted in a change in the visible absorption spectrum of the luminophore[47,51]. In addition, the plot of PL intensity versus the content of Co-2,3-DHTA-COF (Supplementary Fig. 31d) turned out to have upwards curvature when fitted with the Stern−Volmer equation[52], indicating that the PL of $[Ru(bpy)_3]Cl_2$ was not inherently collision quenching[47,52]. Therefore, the quenching of the PL intensity of $[Ru(bpy)_3]Cl_2$ was directly caused by the transfer of photoexcited electrons from $[Ru(bpy)_3]Cl_2$ to Co-2,3-DHTA-COF.

The evidence for this transfer was provided by ultrafast femtosecond time-resolved transient absorption (fs-TA) spectroscopy. As can be seen in Supplementary Fig. 32, after excitation of $[Ru(bpy)_3]Cl_2$, a bleaching peak was observed at approximately 450 nm, and the strength of this peak decreased with increasing delay time, which indicated that the recombination of a fraction of electrons and holes occurred in $[Ru(bpy)_3]Cl_2$ with the prolonged delay time. For Co-2,3-DHTA-COF, the strong and broad photoinduced bleaching peaks were observed at 490 nm and 550−650 nm (Supplementary Fig. 33a), which was attributed to the generation of photoexcited electrons in the conduction band of Co-2,3-DHTA-COF[53,54]. As the delay time increased to 1 ns, these peaks were not observed in Co-2,3-DHTA-COF due to the recombination of electrons and holes. Similar results were obtained for Co-TP-COF and 2,3-DHTA-COF (Supplementary Fig. 33b, c). Nevertheless, when Co-2,3-DHTA-COF was added into the solution of $[Ru(bpy)_3]Cl_2$, the peak strength of Co-2,3-DHTA-COF at approximately 550−650 nm increased with increasing delay time (Supplementary Fig. 32d), indicating that the electron transferred from $[Ru(bpy)_3]Cl_2$ to Co-2,3-DHTA-COF[27,55]. Therefore, the above results suggested that the photoelectrons were transferred from the excited state of $[Ru(bpy)_3]Cl_2$ to Co-COF/COF.

Compared with the COF matrixes, Co-COF displayed more significantly quenched photoluminescence emission and enhanced electron trapping and charge carrier separation. Thus, an adequate supply of electrons was realized by COF with abundant cobalt sites to optimize the elementary process of CO_2 photocatalytic reduction. In addition, the significantly decreased lifetime of $[Ru(bpy)_3]Cl_2$ in the presence of Co-COF/COF also supported favorable electron transfer. Compared with Co-2,3-DHTA-COF, Co-TP-COF exhibited a less pronounced PL quenching effect and leaded to a longer lifetime of $[Ru(bpy)_3]Cl_2$ (173 ns in the presence of Co-TP-COF versus 156 ns in the presence of Co-2,3-DHTA-COF) (Supplementary Fig. 30b), which suggested that the recombination of photogenerated electron and hole pairs was better prevented by Co-2,3-DHTA-COF, and long-lived electrons were provided for CO_2 reduction. For Co-TP-COF and 2,3-DHTA-COF, when $[Ru(bpy)_3]Cl_2$ was added, there was no obvious change in the fs-TA spectra within 7 ns (Supplementary Fig. 33e, f), indicating the rapid recombination of electrons and holes[56,57]. This result further verified that Co-2,3-DHTA-COF induced a high separation efficiency of electron and hole pairs for excited $[Ru(bpy)_3]Cl_2$. Furthermore, the lifetimes of the photogenerated electrons in Co-TP-COF and Co-2,3-DHTA-COF were evaluated by PL decay spectroscopy. By fitting the curves in Supplementary Fig. 34 with a biexponential equation[54], the average lifetime (τ_{avg}) values of photogenerated electrons in Co-2,3-DHTA-COF and Co-TP-COF were calculated to be 3.17 and 2.12 ns, respectively, supporting the result from the steady-state PL measurement. As such, the isolated Co metal sites anchored on 2,3-DHTA-COF facilitated photoinduced electron separation, resulting in enhanced CO_2 photoreduction efficiency.

Next, the surface charge transfer efficiency was measured by electrochemical impedance spectroscopy (EIS) (Supplementary Fig. 35), and the charge transfer resistance simulated by the equivalent circuit followed the sequence Co-2,3-DHTA-COF (23 Ω) < Co-TP-COF (42 Ω) (Supplementary Table 8). Considering that the Co content in 2,3-DHTA-COF was higher than that in Co-TP-COF, this order suggested an inverse relation between interfacial charge transfer resistance and the contents of cobalt sites. Similarly, the Co-COF samples showed lower charge transfer resistance levels than their parent COF matrices. These results were well supported by the transient photocurrent response, where the transient photocurrent density of Co-2,3-DHTA-COF was significantly higher than that of Co-TP-COF, indicating a relatively high charge migration rate (Supplementary Fig. 36). Obviously, cobalt-active centers with different microenvironments played crucial roles in the CO_2 adsorption, electron transportation, and separation of electrons and holes. Therefore, the $Co\text{-}O_4$ sites in Co-2,3-DHTA-COF clearly enabled this Co-COF to provide the high CO_2 adsorption capacity, low charge-transfer resistance, and strong separation of electrons and holes, resulting in high photocatalytic performance of the CO_2RR to CO.

Moreover, in-situ attenuated total reflectance (ATR)-FTIR measurements were performed to study the possible intermediates in CO_2 reduction (Fig. 5a). The strong peaks at 2359 and 2313 cm^{-1} were assigned to the asymmetric stretching of CO_2[16,58]. This is a strong hint that strong CO_2 binding on the surface of Co-2,3-DHTA-COF was the initial step of the catalytic process[58]. The peaks at 1402 and 1455 cm^{-1} were assigned to the symmetric stretching of carbonate CO_3^{2-}[59−62]. Interestingly, with increasing irradiation time, a characteristic peak of *COOH appeared at 1647 cm^{-1}, which was reported to be the most crucial intermediate in the photoreduction process of CO_2 to CO[48]. In addition, the gradually enhanced peak at 2130 cm^{-1} corresponded to the *CO intermediate in the photocatalytic process[63−66], which was the critical intermediate for the formation of the final product CO. Therefore, these results suggested that *COOH and *CO intermediates were involved in the photocatalytic CO_2RR to CO process.

To further clarify the inherent reason for the superior catalytic activity of Co-2,3-DHTA-COF and understand the nature of the active
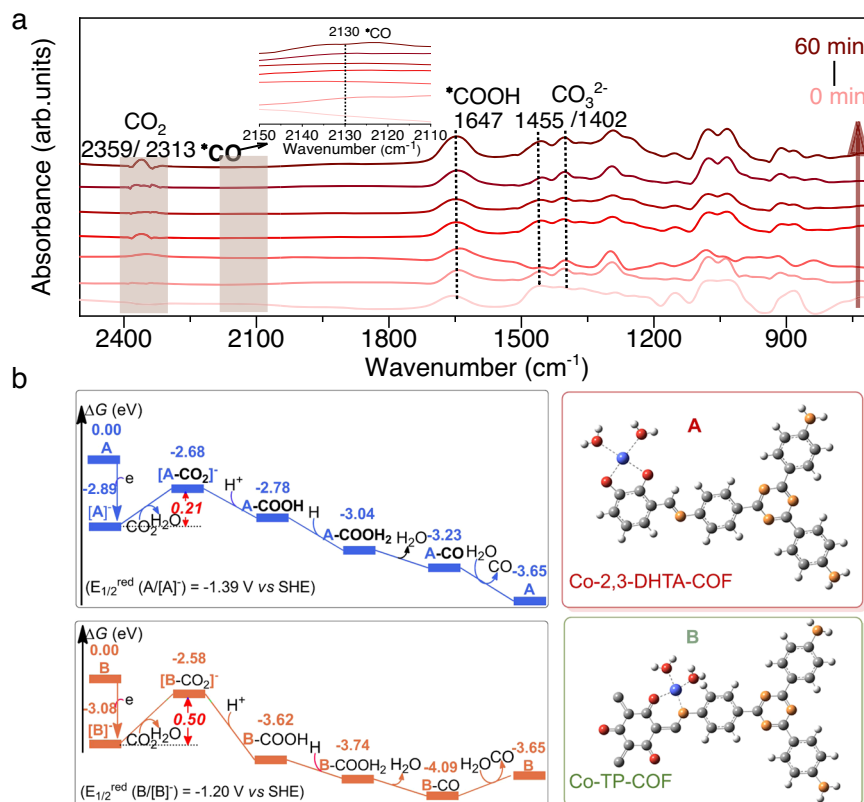
Fig. 5 | In situ ATR-FTIR spectra and reaction Gibbs free energy change. a Room temperature in situ ATR-FTIR spectra of the Co-2,3-DHTA-COF system to detect the formation of intermediates during photoreduction. **b** Gibbs energy profiles of the CO_2RR to CO over Co-2,3-DHTA-COF (A, blue line) and Co-TP-COF (B, orange line).

sites of the catalysts, DFT calculations were performed. For a direct comparison, the single period structures of Co-2,3-DHTA-COF (denoted as A) and Co-TP-COF (denoted as B) were selected as models to explore the reactivity (as shown in Fig. 5b). It should be noted that each A or B molecule contained two H_2O ligands from $Co(NO_3)_2 \cdot 6H_2O$, providing two oxygen atoms to form Co-O coordination.

The calculated results indicated that **A** captured an electron first to form $[\mathbf{A}]^-$ and the redox potential of A ($E_{1/2}^{red}$ ($\mathbf{A}/[\mathbf{A}]^-$)) was −1.39 V (vs. SHE). Then, one H_2O ligand in $[\mathbf{A}]^-$ was replaced by a CO_2 molecule, resulting in the formation of $[\mathbf{A}\text{-}CO_2]^-$. The process of $[\mathbf{A}]^- + CO_2 \rightarrow [\mathbf{A}\text{-}CO_2]^- + H_2O$ was endothermic ($\Delta H = 0.25$ eV), and its ΔG value was 0.21 eV. From $[\mathbf{A}\text{-}CO_2]^-$, one of the O sites of the CO_2 ligand was protonated to form the intermediate **A**-COOH, i.e., *COOH species shown in situ ATR-FTIR. Then, one $H^+ + e^-$ pair (i.e., H atom) attacked the O(H) site to form unstable **A**-$COOH_2$, and one H_2O molecule was dissociated from **A**-$COOH_2$ to generate **A**-CO (intermediate *CO). Finally, ligand exchange occurred between **A**-CO and an H_2O molecule, leading to the release of a CO molecule and the regeneration of the catalyst. The rate-determining step of the CO_2RR catalyzed by A was a ligand exchange process between $[\mathbf{A}]^-$ and CO_2, and its ΔG was 0.21 eV. In addition, we theoretically evaluated the catalytic activity of Co-TP-COF for the CO_2RR to CO and the computation model is presented in Fig. 5b. The rate-determining step for CO_2RR catalyzed by **B** was the ligand exchange process between $[\mathbf{B}]^-$ and CO_2 for the formation of intermediate $[\mathbf{B}\text{-}CO_2]^-$. The ΔG value of $[\mathbf{B}]^- + CO_2 \rightarrow [\mathbf{B}\text{-}CO_2]^- + H_2O$ was 0.50 eV, which was significantly larger than that for **A**. Therefore, the superior catalytic activity of Co-2,3-DHTA-COF occurred due to the lower energy barrier in the ligand exchange process between Co-2,3-DHTA-COF and CO_2.

From the above experimental and theoretical results, a possible mechanism was proposed for the photoreduction of CO_2 to CO catalyzed by Co-2,3-DHTA-COF. Upon visible light irradiation, the photosensitizer $[Ru(bpy)_3]Cl_2$ was excited, and the induced electrons were transferred to the Co-COF catalyst matrix in the Co-O_4 coordination mode. The remaining holes were captured by the electron donor TEOA, which was then oxidized to $TEOA_{ox}^+$, and the entire cycle was closed. The coordination mode in Co-2,3-DHTA-COF accelerated the separation of electrons and holes, and effectively boosted the photocatalytic CO_2 reduction to CO.

Discussion

In summary, we designed Co-O_4 active sites in Co-COF by modulating the position of hydroxyl groups in aldehyde modules under the guidance of a programmable approach. By using the as-designed Co-2,3-DHTA-COF as the catalyst, remarkable photocatalytic CO_2 reduction to CO was achieved with a high CO production rate of 18,000 μmol g^{-1} h^{-1} and excellent selectivity of 95.7%. Notably, a simulation apparatus based on the optimal catalyst showed a CO production rate of 11,000 μmol g^{-1} h^{-1} and a selectivity of 89% under natural sunlight, highlighting the significant importance of Co-O_4 sites in Co-COF for photocatalytic CO_2RR to CO. Furthermore, it was found that a distinctive coordination environment improved the loading capability of Co (II) in the COF, accelerated the electron transfer process from photosensitizer to catalyst, and enhanced CO_2 adsorption capacity, which boosted the catalytic performance. A detailed DFT simulation further revealed that Co-2,3-DHTA-COF enriched with Co-O_4 active sites significantly decreased the energy barrier of the rate-determining step (ligand exchange between Co-2,3-DHTA-COF and CO_2). Therefore, we believed that such a module programmable approach provided a promising way towards optimizing the metal coordination environment of metal-COF for highly efficient CO_2RR and could be applied to design other photocatalysts from reticular nanomaterials.

Methods

Synthesis of 2,3-DHTA-TAPT-COF

In a 10 mL Pyrex tube, TAPT (62.92 mg, 0.174 mmol), 2,3-DHTA (44.08 mg, 0.260 mmol), 1,3,5-trimethylbenzene (3.4 mL), 1,4-dioxane (0.6 mL), and 6 M aqueous acetic acid (0.4 mL) were mixed and sonicated. The tube was degassed via a freeze-pump with liquid nitrogen for three cycles and then heated at 120 °C for 72 h. The produced precipitate was gathered and washed with anhydrous tetrahydrofuran (THF) for further purification. Finally, the red–brown material was obtained with a yield of 80 wt.% by Soxhlet extraction with THF for 24 h and dried under vacuum conditions at 80 °C overnight. Other COF matrixes were synthesized with similar procedures (see Supplementary Information).

Synthesis of Co-2,3-DHTA-COF catalyst

2,3-DHTA-TAPT-COF (50.00 mg) and $Co(NO_3)\cdot6H_2O$ (1.00 g, 3.440 mmol) were added to an ethanol/water mixed solution (v/v = 1:1) and stirred at 95 °C for 24 h. After centrifugation, the product was washed several times with water to ensure the removal of residual metal ions and then dried under vacuum, and its yield was 90 wt.%. The Co-TP-COF catalyst was synthesized with similar methods (see Supplementary Information).

Photocatalytic CO_2 reduction tests

The photocatalytic CO_2 reduction experiments were conducted in a 250 mL optical reaction vessel (PQ256, Beijing Perfect light Technology Co., Ltd) with vigorous stirring in the thermostat at 25 °C. In a typical photocatalytic experiment, 1.00 mg of catalyst was dispersed in 40 mL of acetonitrile/H_2O (v:v = 4:1) mixed solution under ultrasound. Then, 10.00 mg of photosensitizer $[Ru(bpy)_3]Cl_2\cdot6H_2O$ and 6 mL of sacrificial reagent TEOA were dissolved in this mixture. After homogeneous mixing, the reactor was evacuated by a vacuum pump followed by purging with high-purity CO_2 (99.999 vol.%) three times. Afterwards, CO_2 gas was bubbled through the reactor for 30 min to fully saturate the solution at 1 atm. The light source for the photocatalytic reaction was a 300 W Xe lamp (Microsolar 300, cut 420 nm), and the light intensity was 100 mW cm^{-2} (one sun). The production of CO and H_2 was detected by FULI 9790II gas chromatography. After a cycle of photocatalytic reduction, the catalyst was washed with water and then centrifuged for the next run. After adding an equal amount of fresh acetonitrile, H_2O and $[Ru(bpy)_3]Cl_2\cdot6H_2O$, CO_2 was reintroduced to the photocatalytic system under the same operating conditions. In addition, possible liquid products were detected by ^1H NMR spectroscopy (Bruker AVIII HD 600 instrument at 600 MHz). Isotope labeling measurements were performed by using $^{13}CO_2$ gas (enrichment, 99 at.%, Sigma–Aldrich Co., Ltd) as the carbon source, and the gas product was identified by gas chromatography–mass spectrometry (GC–MS, Agilent GC/MS-7000D).

Photoelectrochemical measurements

All photoelectrochemical measurements were conducted by a CHI 760E electrochemical workstation via a standard three-electrode cell. A saturated Ag/AgCl electrode was used as the reference electrode, and a Pt mesh was used as the counter electrode. To prepare the working electrode, appropriate amounts of catalyst sample and Nafion in ethanol were mixed and sonicated, and the mixture was spread evenly on the surface of indium tin oxide (ITO) conductive glass. After air drying, the working electrode was stored in petri dishes for related tests. In this study, an aqueous sodium sulfate solution (0.500 M) was selected as the electrolyte. In the photocurrent test, a 300 W Xe lamp (cut 420 nm) was used as a light source. For EIS measurements, the samples were tested with a frequency range from 10 kHz to 0.1 Hz. Mott-Schottky experimental plots were determined at frequencies of 500, 1000, and 1500 Hz.

In situ ATR-FTIR

The ATR measurement was performed by a Thermo Nicolet iS50 spectrometer (USA) with a mercury cadmium telluride (MCT) detector in the system. In a typical procedure, the samples were dispersed in acetonitrile/H_2O (v:v = 4:1) with $[Ru(bpy)_3]Cl_2\cdot6H_2O$ and TEOA before sealing in the chamber for purging with N_2 for 1 h. Typical signals of two intermediates were captured after the introduction of flowing CO_2 under dark (10 min) and light irradiation (0–60 min) conditions.

X-ray absorption fine structure (XAFS) spectroscopy

XAFS spectra (Co K-edge) were collected at the 1W1B station in the Beijing Synchrotron Radiation Facility (BSRF). The storage rings of BSRF were operated at 4–23 KeV. By using a Si(111) double-crystal monochromator, the data were collected in transmission mode using an ionization chamber (i.e., Co foil, CoO, Co_3O_4, and CoPc). The energy resolution of the spectrometer was approximately 1.4 eV, providing an overall energy resolution of approximately 1.5 eV at the Co K-edge, including core-hole effects. To obtain the quantitative structural parameters around central atoms, data processing was conducted by using Athena and Artemis software from the IFEFFIT package.

Data availability

The data that support the findings of this study are available in the paper and Supplementary Information. Source data are provided with this paper.

References

1. Davis, S. J., Caldeira, K. & Matthews, H. D. Future CO_2 emissions and climate change from existing energy infrastructure. *Science* **329**, 1330–1333 (2010).
2. Shindell, D. & Smith, C. J. Climate and air-quality benefits of a realistic phase-out of fossil fuels. *Nature* **573**, 408–411 (2019).
3. Zhang, X. et al. Assisting Bi_2MoO_6 microspheres with phenolic resin-based ACSs as attractive tailor-made supporter for highly-efficient photocatalytic CO_2 reduction. *Green Energy Environ.* **6**, 693–702 (2021).
4. Zhang, J. H., Zhong, D. C. & Lu, T. B. Co (II)-based molecular complexes for photochemical CO_2 reduction. *Acta Phys. Chim. Sin.* **37**, 1–15 (2021).
5. Lee, Y. Y., Jung, H. S. & Kang, Y. T. A review: effect of nanostructures on photocatalytic CO_2 conversion over metal oxides and compound semiconductors. *J. CO_2 Util.* **20**, 163–177 (2017).
6. Wang, S. et al. Inside-and-out semiconductor engineering for CO_2 photoreduction: from recent advances to new trends. *Small Struct.* **2**, 2000061 (2021).
7. Bie, C., Zhu, B., Xu, F., Zhang, L. & Yu, J. In situ grown monolayer N-doped graphene on CdS hollow spheres with seamless contact for photocatalytic CO_2 reduction. *Adv. Mater.* **31**, 1902868 (2019).
8. Liu, Y. et al. Polyoxometalate@metal-organic framework composites as effective photocalysts. *ACS Catal.* **11**, 13374–13396 (2021).
9. Zhong, H. et al. A phthalocyanine-based layered two-dimensional conjugated metal-organic framework as a highly efficient electrocatalyst for the oxygen reduction reaction. *Angew. Chem. Int. Ed.* **58**, 10677–10682 (2019).
10. Dong, X. Y., Si, Y. N., Wang, Q. Y., Wang, S. & Zang, S. Q. Integrating single atoms with different microenvironments into one porous organic polymer for efficient photocatalytic CO_2 reduction. *Adv. Mater.* **33**, 2101568 (2021).
11. Xia, C. L. et al. The emerging covalent organic frameworks (COFs) for solar-driven fuels production. *Coord. Chem. Rev.* **446**, 214117 (2021).
12. Meng, Z. & Mirica, K. A. Covalent organic frameworks as multifunctional materials for chemical detection. *Chem. Soc. Rev.* **50**, 13498–13558 (2021).

13. Yang, S. et al. 2D covalent organic frameworks as intrinsic photocatalysts for visible light-driven CO_2 reduction. *J. Am. Chem. Soc.* **140**, 14614–14618 (2018).

14. Ma, T. Q. et al. Single-crystal x-ray diffraction structures of covalent organic frameworks. *Science* **361**, 48–52 (2018).

15. Yang, S. et al. Microenvironments enabled by covalent organic framework linkages for modulating active metal species in photocatalytic CO_2 reduction. *Adv. Funct. Mater.* **32**, 2110694 (2022).

16. Cheng, L. et al. Dual-single-atom tailoring with bifunctional integration for high-performance CO_2 photoreduction. *Adv. Mater.* **33**, 2105135 (2021).

17. Wu, Q. et al. Integration of strong electron transporter tetrathiafulvalene into metalloporphyrin-based covalent organic framework for highly efficient electroreduction of CO_2. *ACS Energy Lett.* **5**, 1005–1012 (2020).

18. Kim, H. et al. Identification of single-atom Ni site active toward electrochemical CO_2 conversion to CO. *J. Am. Chem. Soc.* **143**, 925–933 (2021).

19. Li, Y. et al. Facile top-down strategy for direct metal atomization and coordination achieving a high turnover number in CO_2 photoreduction. *J. Am. Chem. Soc.* **142**, 19259–19267 (2020).

20. Li, M. et al. Heterogeneous single-atom catalysts for electrochemical CO_2 reduction reaction. *Adv. Mater.* **32**, 2001848 (2020).

21. Shen, Y. et al. Programmable logic in metal-organic frameworks for catalysis. *Adv. Mater.* **33**, 2007442 (2021).

22. Li, H., Wang, L. & Yu, G. Covalent organic frameworks: design, synthesis, and performance for photocatalytic applications. *Nano Today* **40**, 101247 (2021).

23. Cui, X. et al. Emerging covalent organic frameworks tailored materials for electrocatalysis. *Nano Energy* **70**, 104525 (2020).

24. Xin, W. et al. Tunable molecular transport and sieving enabled by covalent organic framework with programmable surface charge. *Mater. Today* **51**, 56–64 (2021).

25. Li, Y. et al. One-dimensional superlattice heterostructure library. *J. Am. Chem. Soc.* **143**, 7013–7020 (2021).

26. Gong, Y. N. et al. Regulating photocatalysis by spin-state manipulation of cobalt in covalent organic frameworks. *J. Am. Chem. Soc.* **142**, 16723–16731 (2020).

27. Liu, W. et al. A scalable general synthetic approach toward ultrathin imine-linked two-dimensional covalent organic framework nanosheets for photocatalytic CO_2 reduction. *J. Am. Chem. Soc.* **141**, 17431–17440 (2019).

28. Zhong, W. et al. A covalent organic framework bearing single Ni sites as a synergistic photocatalyst for selective photoreduction of CO_2 to CO. *J. Am. Chem. Soc.* **141**, 7615–7621 (2019).

29. Xu, T. et al. Covalent organic framework with triazine and hydroxyl bifunctional groups for efficient removal of lead(II) Ions. *Ind. Eng. Chem. Res.* **58**, 19642–19648 (2019).

30. Yang, Y. et al. Decoration of active sites in covalent-organic framework: an effective strategy of building efficient photocatalysis for CO_2 reduction. *ACS Sustain. Chem. Eng.* **9**, 13376–13384 (2021).

31. Butler, M., Mañez, P. A., Cabrera, G. M. & Maître, P. Gas phase structure and reactivity of doubly charged microhydrated calcium(II)-catechol complexes probed by infrared spectroscopy. *J. Phys. Chem. A* **118**, 4942–4954 (2014).

32. Lana-Villarreal, T., Rodes, A., Pérez, J. M. & Gómez, R. A Spectroscopic and electrochemical approach to the study of the interactions and photoinduced electron transfer between catechol and anatase nanoparticles in aqueous solution. *J. Am. Chem. Soc.* **127**, 12601–12611 (2005).

33. Das, S. K. et al. CuO grafted triazine functionalized covalent organic framework as an efficient catalyst for C-C homo coupling reaction. *Mol. Catal.* **480**, 110650 (2020).

34. Halder, A. et al. Decoding the morphological diversity in two dimensional crystalline porous polymers by core planarity modulation. *Angew. Chem. Int. Ed.* **55**, 7806–7810 (2016).

35. Niu, Q. et al. Rational design of novel COF/MOF s-scheme heterojunction photocatalyst for boosting CO_2 reduction at gas-solid interface. *ACS Appl. Mater. Interfaces* **14**, 24299–24308 (2022).

36. Yang, R. et al. Potential difference-modulated synthesis of self-standing covalent organic framework membranes at liquid/liquid interfaces. *J. Am. Chem. Soc.* **144**, 11778–11787 (2022).

37. Aduru, S., Contarini, S. & Rabalais, J. W. Electron-, x-ray-, and ion-stimulated decomposition of nitrate salts. *J. Phys. Chem.* **90**, 1683–1688 (1986).

38. Tolman, C. A., Riggs, W. M., Linn, W. J., King, C. M. & Wendt, R. C. Electron spectroscopy for chemical analysis of nickel compounds. *Inorg. Chem.* **12**, 2770–2778 (1973).

39. Li, L. H. et al. Salen-based covalent organic framework. *J. Am. Chem. Soc.* **139**, 6042–6045 (2017).

40. Wang, X. et al. Covalent organic framework nanosheets embedding single cobalt sites for photocatalytic reduction of carbon dioxide. *Chem. Mater.* **32**, 9107–9114 (2020).

41. El-Sonbati, A. Z. et al. Synthesis, characterization of Schiff base metal complexes and their biological investigation. *Appl. Organomet. Chem.* **33**, e5048 (2019).

42. Deghadi, R. G., Mahmoud, W. H. & Mohamed, G. G. Metal complexes of tetradentate azo-dye ligand derived from 4,4'-oxydianiline: preparation, structural investigation, biological evaluation and MOE studies. *Appl. Organomet. Chem.* **34**, e5883 (2020).

43. Mohamed, A. A. & Sadeek, S. A. Ligational and biological studies of Fe(III), Co (II), Ni(II), Cu(II), and Zr(IV) complexes with carbamazepine as antiepileptic drug. *Appl. Organomet. Chem.* **35**, e6178 (2021).

44. Niu, P., Pan, Z., Wang, S. & Wang, X. Tuning crystallinity and surface hydrophobicity of a cobalt phosphide cocatalyst to boost CO_2 photoreduction performance. *ChemSusChem* **14**, 1302–1307 (2021).

45. Boston, D. J., Xu, C., Armstrong, D. W. & MacDonnell, F. M. Photochemical reduction of carbon dioxide to methanol and formate in a homogeneous system with pyridinium catalysts. *J. Am. Chem. Soc.* **135**, 16252–16255 (2013).

46. Gao, C. et al. Co_3O_4 Hexagonal platelets with controllable facets enabling highly efficient visible-light photocatalytic reduction of CO_2. *Adv. Mater.* **28**, 6485–6490 (2016).

47. Gao, C. et al. Heterogeneous single-atom catalyst for visible-light-driven high-turnover CO_2 reduction: the role of electron transfer. *Adv. Mater.* **30**, 1704624 (2018).

48. Guo, D. et al. Effects of extrinsic defects originating from the interfacial reaction of CeO_2-x-nickel silicate on catalytic performance in methane dry reforming. *Appl. Catal. B-Environ.* **277**, 119278 (2020).

49. Yao, L., Galvez, M. E., Hu, C. & Da Costa, P. Synthesis gas production via dry reforming of methane over manganese promoted nickel/cerium-zirconium oxide catalyst. *Ind. Eng. Chem. Res.* **57**, 16645–16656 (2018).

50. Wang, Z. et al. Room-temperature synthesis of single iron site by electrofiltration for photoreduction of CO_2 into tunable syngas. *ACS Nano* **14**, 6164–6172 (2020).

51. Barry, R. M. Principles of fluorescence spectroscopy, Third Edition. *J. Biomed. Opt.* **13**, 029901 (2008).

52. Cokoja, M., Bruckmeier, C., Rieger, B., Herrmann, W. A. & Kühn, F. E. Transformation of carbon dioxide with homogeneous transition-metal catalysts: a molecular solution to a global challenge? *Angew. Chem. Int. Ed.* **50**, 8510–8537 (2011).

53. Li, C., Wang, H., Naghadeh, S. B., Zhang, J. Z. & Fang, P. Visible light driven hydrogen evolution by photocatalytic reforming of lignin and lactic acid using one-dimensional NiS/CdS nanostructures. *Appl. Catal. B-Environ.* **227**, 229–239 (2018).

54. Ran, L. et al. Engineering single-atom active sites on covalent organic frameworks for boosting CO_2 photoreduction. *J. Am. Chem. Soc.* **144**, 17097–17109 (2022).

55. Tran, T. T. et al. Snapshots of light induced accumulation of two charges on methylviologen using a sequential nanosecond pump-pump photoexcitation. *J. Phys. Chem. Lett.* **9**, 1086–1091 (2018).

56. Guo, S. et al. Robust and long-lived excited state Ru(II) polyimine photosensitizers boost hydrogen production. *ACS Catal.* **8**, 8659–8670 (2018).

57. Li, Y., Xie, W. & Jiang, X. Mechanistic study of a photocatalyzed C-S bond formation involving alkyl/aryl thiosulfate. *Chem. Eur. J.* **21**, 16059–16065 (2015).

58. Guo, S., Xiao, Y. & Jiang, B. Encapsulation of Pd nanoparticles in covalent triazine frameworks for enhanced photocatalytic CO_2 conversion. *ACS Sustain. Chem. Eng.* **9**, 12646–12654 (2021).

59. Wang, T. et al. Photoreduction of CO_2 over the well-crystallized ordered mesoporous TiO_2 with the confined space effect. *Nano Energy* **9**, 50–60 (2014).

60. Li, N. et al. Toward high-value hydrocarbon generation by photocatalytic reduction of CO_2 in water vapor. *ACS Catal.* **9**, 5590–5602 (2019).

61. Cai, X. et al. Tuning selectivity in catalytic conversion of CO_2 by one-atom-switching of Au_9 and Au_8Pd_1 catalysts. *CCS Chem.* **3**, 408–420 (2021).

62. Jiang, M. P. et al. Magnetic-field-regulated TiO_2 {100} facets: a strategy for C-C coupling in CO_2 photocatalytic conversion. *Chem* **6**, 2335–2346 (2020).

63. Li, J. et al. Self-adaptive dual-metal-site pairs in metal-organic frameworks for selective CO_2 photoreduction to CH_4. *Nat. Catal.* **4**, 719–729 (2021).

64. Li, X. D. et al. Selective visible-light-driven photocatalytic CO_2 reduction to CH_4 mediated by atomically thin $CuIn_5S_8$ layers. *Nat. Energy* **4**, 690–699 (2019).

65. Xiang, S. et al. Microporous metal-organic framework with potential for carbon dioxide capture at ambient conditions. *Nat. Commun.* **3**, 954 (2012).

66. Li, X. Sp^2 carbon-conjugated covalent organic frameworks: synthesis, properties, and applications. *Mater. Chem. Front.* **5**, 2931–2949 (2021).

Acknowledgements

Author contributions

J.J. W., Z.M. L., H.Y. W., and Q. Z. designed the experiments. Q. Z. and S.Q. G. performed the experiments and analyzed the data. Y.Y. G. completed some synthesis experiments. X.F. S. provided the DFT calculation support. Q. Z., J.S. W., H.Y. W., J.J. W., H.C. Z., and Z.M. L. wrote the manuscript. All authors discussed the results and commented on the manuscript.

Competing interests

The authors declare no competing interests.

Additional information

Supplementary information The online version contains supplementary material available at https://doi.org/10.1038/s41467-023-36779-4.

Correspondence and requests for materials should be addressed to Huiyong Wang, Zhimin Liu or Jianji Wang.

Peer review information *Nature Communications* thanks the anonymous reviewers for their contribution to the peer review of this work.

Reprints and permissions information is available at http://www.nature.com/reprints

Publisher's note Springer Nature remains neutral with regard to jurisdictional claims in published maps and institutional affiliations.